Rapid whole brain imaging of neural activities in freely behaving larval zebrafish

Lin Cong[1,4], Zeguan Wang[2,4], Yuming Chai[2,4], Wei Hang[1,4], Chunfeng Shang[1], Wenbin Yang[2], Lu Bai[1], Jiulin Du[1], Kai Wang[1,3], Quan Wen[2]

1. Institute of Neuroscience, State Key Laboratory of Neuroscience, CAS Center for Excellence in Brain Science and Intelligence Technology, Chinese Academy of Sciences, Shanghai 200031, China.

2. Chinese Academy of Sciences Key Laboratory of Brain Function and Disease, School of Life Sciences, Center for Excellence in Brain Science and Intelligence Technology, University of Science and Technology of China, Hefei, 230027, China.

3. University of Chinese Academy of Sciences, Beijing 100049, China.

4. These authors contributed equally to this work.

Correspondence should be addressed to K.W. (wangkai@ion.ac.cn) or Q.W. (qwen@ustc.edu.cn).

1 **Abstract:**

2 The internal brain dynamics that links sensation and action is arguably better studied

3 during animal's natural behaviors. Here we report novel volume imaging and 3D tracking

4 techniques that perform whole brain imaging of neural activities in freely swimming

5 larval zebrafish. We demonstrated the capability of our system through functional

6 imaging of neural activities during visually evoked behavior and prey capture behavior in

7 larval zebrafish.

8

1 Main text:

2 Introduction:

3 A central goal in systems neuroscience is to understand how distributed neural circuitry

4 dynamics drives animal behaviors. The emerging field of optical neurophysiology allows

5 monitoring [1, 2] and manipulating [3-5] the activities of defined populations of neurons

6 that express genetically encoded activity indicators [6, 7] and light-activated proteins [1,

7 4, 5, 8]. Larval zebrafish has become an attractive model system to investigate the neural

8 correlates of behaviors owing to its small brain size, optical transparency and rich

9 behavioral repertoire [9, 10]. In particular, whole brain imaging of larval zebrafish using

10 light sheet/two-photon microscope holds the promise of creating a comprehensive

11 functional map that links neuronal activities and behaviors [11-13].

12

13 Recording neural activity map in larval zebrafish has been successfully integrated with

14 the virtual reality paradigm: closed-loop fictive behaviors in immobilized fish can be

15 monitored and controlled via visual feedback that varies according to the electrical output

16 patterns of motor neurons [11, 14]. The behavioral repertoire, however, may be further

17 expanded in freely swimming zebrafish whose behavioral states can be directly inferred

18 and when sensory feedback loops are mostly intact and active. For example, it is likely

19 that vestibular as well as proprioceptive feedbacks are perturbed in immobilized zebrafish

20 [14, 15]. The crowning moment during the hunting behavior [16-18] — when a fish

21 succeeds in catching a paramecium — could not be easily replicated in a virtual reality

22 setting. Therefore, whole brain imaging in a freely swimming zebrafish may allow optical

23 interrogation of brain circuits underlying a range of less explored behaviors.

1

2 Although whole brain functional imaging methods are available for head-fixed larval

3 zebrafish, imaging a speeding brain imposes many more technical challenges. Current

4 studies on freely swimming zebrafish were either limited to non-imaging optical system

5 [19] or wide field imaging at low resolution [20]. While the Light Sheet Microscope

6 (LSM) has demonstrated entire brain coverage and single neuron resolution in restrained

7 zebrafish [12], it lacks the speed to follow rapid fish movement. Moreover, in LSM, the

8 sample is illuminated from its side, a configuration that is difficult to be integrated with a

9 tracking system. The conventional Light Field Microscope (LFM) [21, 22] is a promising

10 alternative because of its higher imaging speed, but its spatial resolution is relatively low.

11 A specialized LFM for monitoring neural activities using compressed sensing was

12 developed recently [23], but it relies on spatiotemporal sparsity of fluorescent signals and

13 cannot be applied to moving animals.

14

15 Here, we describe a fast 3D tracking technique and a novel volume imaging method that

16 allow whole brain calcium imaging with high spatial and temporal resolution in freely

17 behaving larval zebrafish. Zebrafish larva possesses extraordinary mobility. It can move

18 at an instantaneous velocity up to 50 mm/s [24] and acceleration of 1g. To continuously

19 track fish motion, we have developed a high-speed closed-loop system in which (1)

20 customized machine vision software allows rapid estimate of fish movement both in X-Y

21 directions and Z direction; (2) feedback control signals drive a high-speed motorized X-Y

22 stage (at 300 Hz) and piezo Z stage (at 100 Hz) to retain the entire fish head within the

23 field of view of a high NA (25x, NA=1.05) objective.

1

2   A larval zebrafish sometimes makes blistering and unpredictable movement that can

3   easily cause motion blur and severely degrade the imaging quality. To overcome this

4   obstacle, we developed a new type of Light Field Microscope: eXtended field of view

5   LFM (XLFM). XLFM can simultaneously image the whole brain neural activities (over a

6   volume of 800 μm × 800 μm × 200 μm) at ~ 3.4 μm × 3.4 μm × 5 μm spatial resolution

7   and at 77 Hz volume rate，with the aid of genetically encoded calcium indicator

8   GCamp6f. Furthermore, the implementation of flashed fluorescence excitation (200 μs in

9   duration) allows blur-free fluorescent images to be captured when a zebrafish moves at a

10   speed up to 10 mm/s. The seamless integration of the tracking and the imaging system

11   makes it possible to reveal rich whole brain neural dynamics during natural behavior with

12   unprecedented resolution. We demonstrated the ability of our system during visually

13   evoked behavior and prey capture in larval zebrafish.

14

Results:

16   The newly developed XLFM is based on the general principle of light field [25] and can

17   acquire 3D information from a single camera frame. The major advancement made by

18   XLFM is the greatly relaxed constrains imposed by counteraction between spatial

19   resolution and imaging volume coverage requirements in conventional LFM. This

20   achievement relies on a few new techniques both in optics and in computational

21   reconstruction method. First, a customized lenslet array (Figure 1a, Supplementary

22   Figure 1) was placed at the rear pupil plane of the imaging objective, instead of being

23   placed at the imaging plane as in LFM. Therefore, spatially invariant point spread

1   function (PSF) of the entire optical imaging system can be defined and measured

2   (Supplementary Figure 2). Second, the aperture size of each micro-lens was decoupled

3   from their interspacing and the spatial arrangement, so both the imaging volume and

4   resolution can be optimized simultaneously given the limited imaging sensor size. Third,

5   multifocal imaging [26, 27] was introduced to further increase the depth of view by

6   dividing micro-lens array into several groups whose focal planes were at different axial

7   positions (Figure 1b & c, Supplementary Figure 3 & 4). Forth, a new computational

8   algorithm based on optical wave theory was developed to accurately reconstruct the

9   entire 3D volume (see Methods).

10

11   We characterized the XLFM by imaging 0.5 μm diameter fluorescent beads. The

12   resolution can be preserved around 3.4 μm × 3.4 μm × 5 μm within the imaging volume

13   of 800 μm × 800 μm × 200 μm (Supplementary Figure 5) when Signal-to-Noise Ratio

14   (SNR) was high and dropped gradually outside this volume (Supplementary Figures 5-6,

15   Methods). For *in vivo* experiments where complex optical properties of biological tissue

16   come into play [28], the achievable resolution could be degraded. We demonstrated the

17   capabilities of XLFM by imaging the whole brain neuronal activities of a larval zebrafish

18   (5 d.p.f) at a speed of 77 volumes/s and at relatively low excitation laser exposure of 2.5

19   mW/mm^2 (Figure 1d, Supplementary Video 1). The zebrafish, which expressed pan-

20   neuronal GCamp6f, was imaged continuously for more than 300,000 volumes without

21   severe photo bleaching (Supplementary Figure 7, Supplementary Video 2 & 3). To test

22   whether XLFM could monitor fast changes in neuronal dynamics across whole brain at

23   high resolution close to single neuron level, we first presented the larval zebrafish,

1   restrained in low melting point agarose, with visual stimulation (~ 2.6 sec duration). We

2   found that different groups of neurons in the forebrain, midbrain and hindbrain were

3   activated at different times (Figure 1e-f, Supplementary Video 1 & 4), suggesting rapid

4   sensorimotor transformation across different brain regions.

5
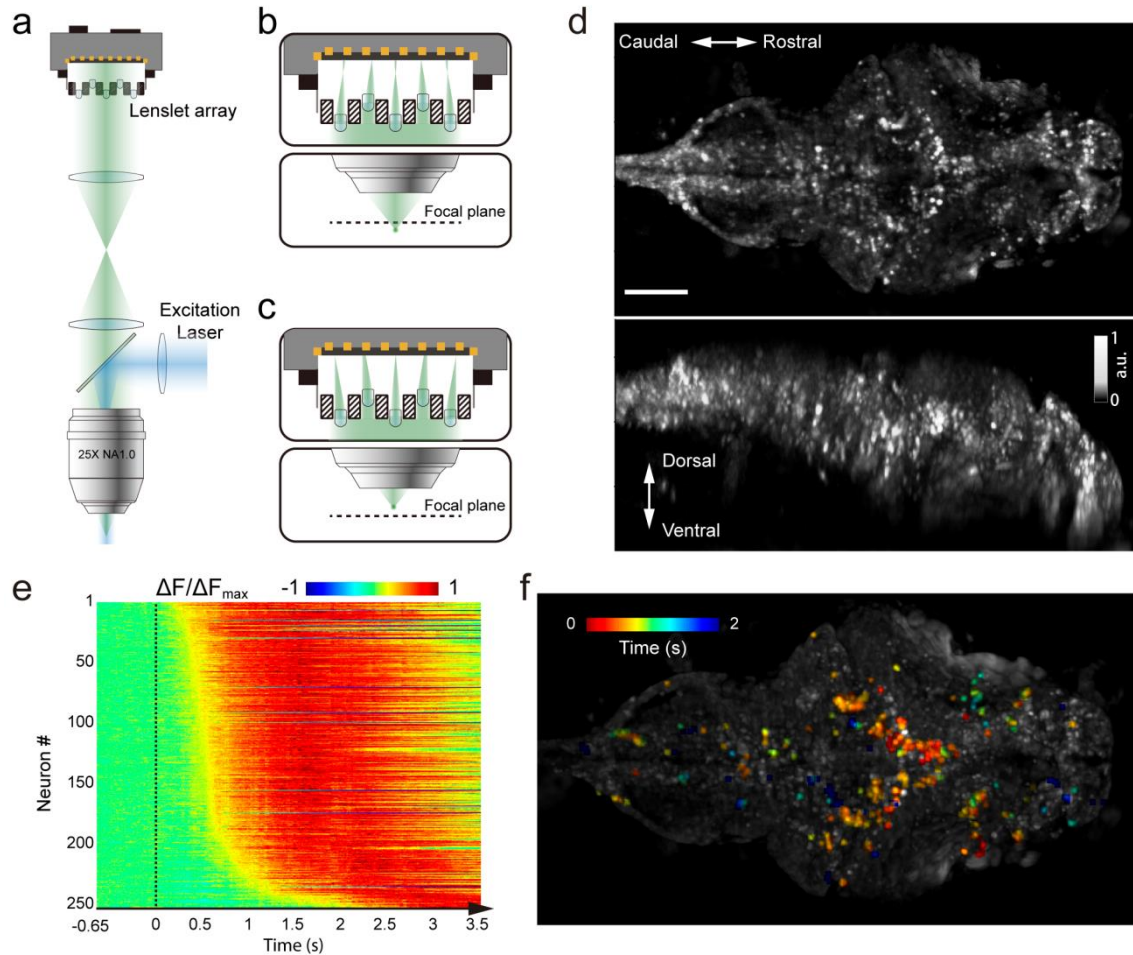
1

2 Figure 1. Whole brain imaging of larval zebrafish with XLFM. (a) Schematic design of XLFM. The

3 position of lenslet array is conjugate to the rear pupil plane of the imaging objective. Excitation laser

4 (blue) provides uniform illumination across the sample. (b-c) Point sources at two different depths will

5 form, through two different groups of microlenses, sharp images on the imaging sensor, and the

6 positional information can be reconstructed from these distinct patterns. (d) Maximum Intensity

7 Projections (MIPs) of pan-neuronal nucleus-localized GCaMP6f fluorescence images from a

8 restrained larval zebrafish. (e) Normalized neuronal activities of selected neurons that exhibited

9 increasing calcium responses after onset of light stimulation at t=0. Neurons were ordered by the onset

10 time when the measured fluorescence signals reached 20% of their maximum. (f) The selected

11 neurons in (e) were also color coded based on their response onset time. Scale bar is 100 μm.

12

1   To track freely swimming larval zebrafish, we transferred fish into a water-filled chamber

2   with glass ceiling and floor. The chamber, 20 mm × 20 mm × 0.8 mm in size, was

3   coupled with a piezo actuator and mounted on a high-speed 2D motorized stage (Figure

4   2). A tracking camera monitored the lateral movement of the fish, and an autofocus

5   camera, which captured light field images of the fish, monitored the axial movement of

6   the fish head (Figure 2, Supplementary Figure 8).

7
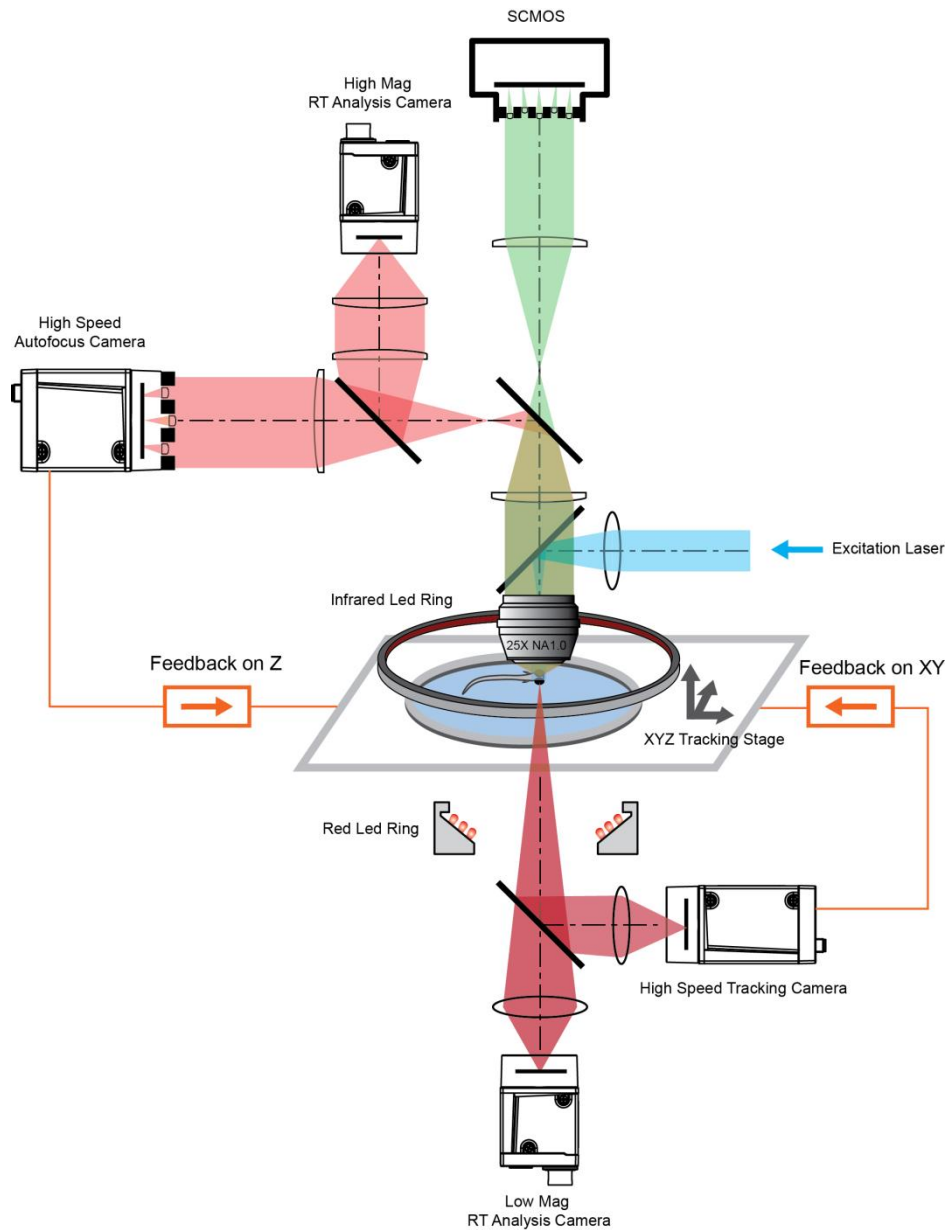
1

2   Figure 2. System schematics that integrates tracking, whole brain functional imaging, and real time

3   behavioral analysis. Larval zebrafish was swimming in a customized chamber with optically

4   transparent ceiling and floor. The water-filled chamber was mounted on a high-speed 3-axis stage (PI

5   M686 & PI P725KHDS). Customized LED rings generated dark field illumination of the zebrafish.

6   The scattered light was collected by four cameras: two cameras below the chamber were used for X-Y

7   plane tracking and low magnification RT analysis respectively; two cameras above the chamber and

8   after the imaging objective were used for Z autofocus and high magnification RT analysis. The

1   positional information of the larval zebrafish, acquired from the tracking and autofocus system, was

2   converted to feedback voltage signals to drive the 3-axis stage and to compensate fish movement. The

3   functional imaging system, described in Figure 1, shared the same imaging objective placed above the

4   swimming chamber. The 3D tracking, RT behavioral analysis and functional imaging systems were

5   synchronized for accurate correlation between neural activities and behavioral output.

6

7   Real-time machine vision algorithms allowed quick estimate of lateral (within 1 ms) and

8   axial (~ 5 ms) head position (see Methods). The error signals in three dimensions, defined

9   as the difference between the head position and the set point, were calculated (Figure 3a)

10   and converted to analog voltage signals through Proportional–Integral–Derivative (PID)

11   control to drive the motorized stage and the z piezo scanner. Tracking and autofocusing

12   allowed rapid compensation of 3D fish movement (300 Hz in x and y, 100 Hz in z,

13   Figure 3a) and retainment of the fish head within the field of view of the imaging

14   objective.

15

16   Our tracking system permitted high-speed and high-resolution recording of larval

17   zebrafish behaviors. With two cameras acquiring head and whole body videos

18   simultaneously (Figure 2, Figure 3b), we recorded and analyzed in real time (see

19   Methods) the kinematics of key features during the larval zebrafish prey capture (Figure

20   3b & c, Supplementary Video 5 & 6). Consistent with several earlier findings [16-18],

21   eye converged rapidly when the fish entered the prey capture state (Figure 3c). Other

22   features that characterized tail and fin movement were also analyzed at high temporal

23   resolution (Figure 3c).

24
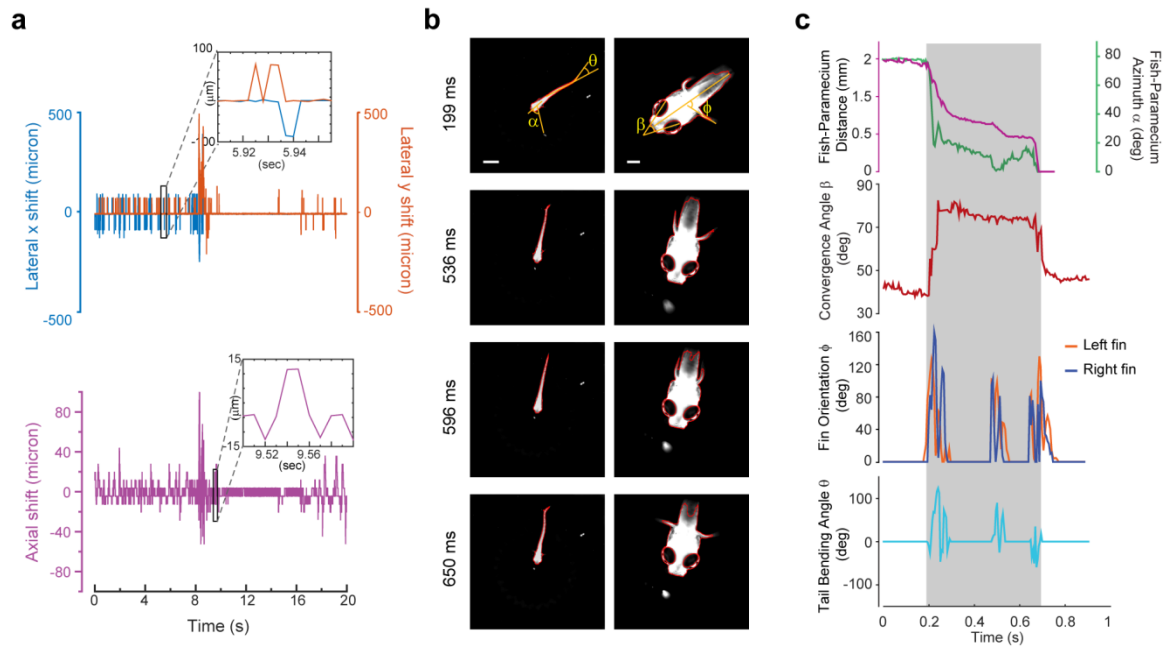
1

2 Figure 3. 3D Tracking of larval zebrafish. (a) Representative time varying error signals in three

3 dimensions, defined as the difference between the real head position and the set point. Inset provides

4 magnified view at short time interval. Lateral movement can be rapidly compensated within a few

5 milliseconds when the fish's instantaneous velocity is up to 10 mm/s. The axial shift was small

6 compared to the depth coverage (200 μm) during whole brain imaging, and thereby would have minor

7 effect on brain activity reconstruction. (b) Tracking images at 4 consecutive time points during prey

8 capture behavior, acquired at low (left) and high (right) magnification simultaneously. Scale bar is 1

9 mm (left) and 200 μm (right). (c) Kinematics of behavioral features during prey capture. Shaded

10 region marks the beginning and the end of the prey capture process.

11

1   The integration of XLFM and 3D tracking system allowed us to perform whole brain

2   functional imaging of a freely behaving larval zebrafish (Figure 2). We first replicated the

3   light-evoked experiment (similar to Figure 1), albeit in a freely behaving zebrafish with

4   pan-neuronal cytoplasm-labeled GCamp6s (Supplementary Video 7), which exhibited

5   faster and more prominent calcium response. Strong activities were observed in the

6   neuropil of optical tectum and the midbrain after stimulus onset. The fish tried to avoid

7   strong light exposure and made fierce tail movement at ~ 60 Hz. Whole brain neural

8   activities were monitored continuously during the light-evoked behavior except for

9   occasional blurred frames due to the limited speed and acceleration of tracking stages.

10

11   Next, we, for the first time, captured whole brain neural activities during the entire prey

12   capture process in freely swimming larval zebrafish (Supplementary Video 8). When a

13   paramecium moved into the visual field of the fish, groups of neurons, as indicated as

14   group 1 in Figure 4b, near the contralateral optical tectum of the fish were first activated

15   (t_1). The fish then converged its eyes onto the paramecium and changed its heading

16   direction to approach the paramecium (t_2). Starting from t_2, several groups of neurons in

17   hypothalamus, midbrain and hindbrain, as highlighted as group 2, 3 and 4 in Figure 4b,

18   were activated. It took the fish *three* attempts (Figure 4c) to catch and eat the paramecium.

19   After the last try (t_4), group 1 neurons' activities decreased gradually, while the activities

20   in other groups of neurons continued to rise and persisted for ~ 1s before the calcium

21   signals decreased. The earliest tectal activity (group 1) responsible for prey detection is

22   consistent with previous studies [29, 30]. Moreover, owing to the technical advancement,

23   our data revealed interesting neural dynamics arising from the other brain regions during

1   and after a successful prey capture. We also monitored similar behavior, in a zebrafish

2   expressing nucleus-localized GCamp6f, with better resolution, but with less prominent

3   calcium response (Supplementary Video 9).

4
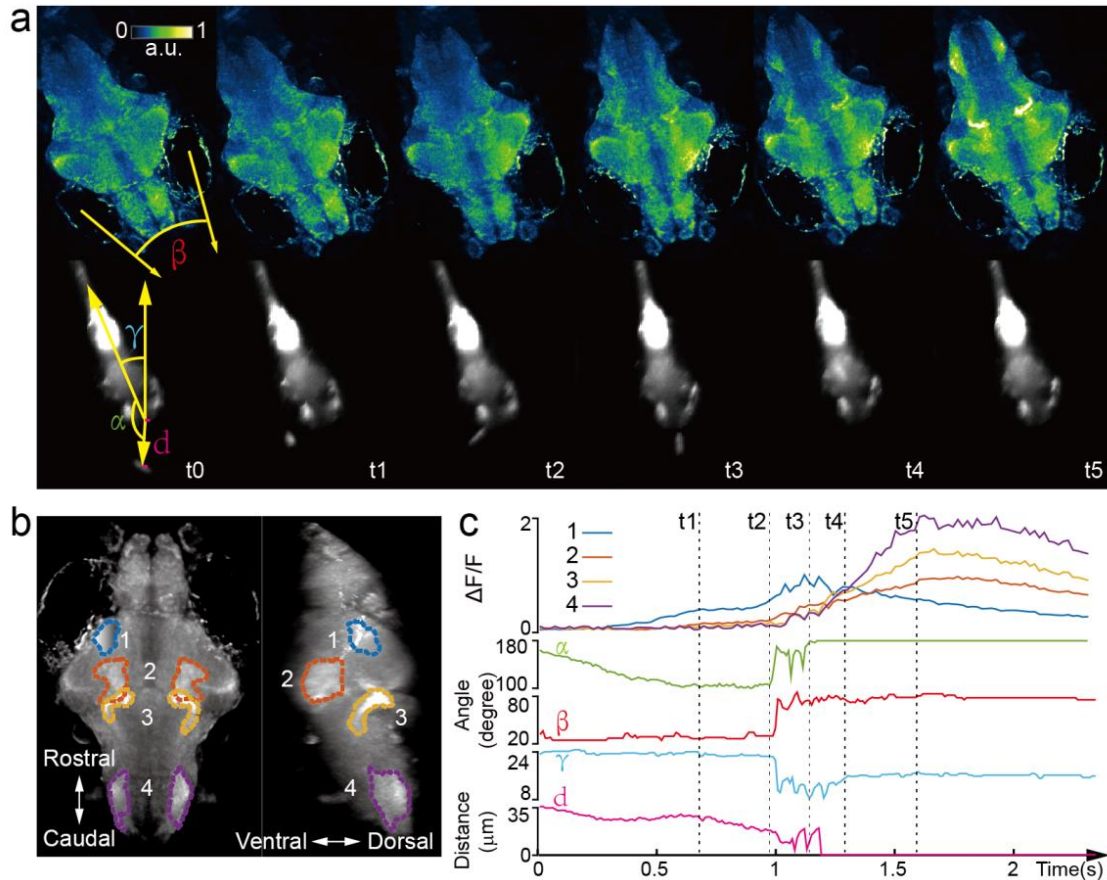
5

6   Figure 4. Whole brain imaging of larval zebrafish during prey capture behavior. (a) Renderings of

7   whole brain calcium activity at six consecutive time points (up) and the corresponding behavioral

8   images (bottom). Features used to quantify the behavior are: fish-paramecium azimuth α; convergence

9   angle between eyes β; head orientation γ; fish-paramecium distance d. (b) MIPs of zebrafish brain

10   with pan-neuronal cytoplasm-labeled GCaMP6f. Boundaries of four brain regions are color marked. (c)

11   Neural dynamics inferred from GCaMP6 fluorescence changes in these four regions during the entire

12   prey capture behavior (up) and the kinematics of behavioral features (bottom). Note that between t2

1   and t4, fish-paramecium distance *d* exhibits three abrupt kinks, representing fish's three attempts to

2   catch the prey.

3

4   **Discussion:**

5   Whole brain imaging in freely behaving animal has been previously reported in another

6   model system, *C. elegans*, by integrating the spinning-disk confocal microscopy with a

7   2D tracking system [31, 32]. In the more remote past, Howard Berg pioneered the use of

8   3D tracking microscopy to study bacteria chemotaxis [33]. However, the significant

9   increase of animal size imposes challenges both on tracking and imaging technologies. In

10   particular, the XLFM, derived from the general concept of light field imaging [21, 25, 34,

11   35], overcomes several critical limitations in the conventional LFM and allows

12   optimization of imaging volume, resolution and speed simultaneously. Furthermore, it

13   can be perfectly combined with flashed fluorescence excitation to capture blur-free

14   images at high resolution during rapid fish movement. Taken together, we have

15   developed a whole brain imaging and tracking microscopy suitable for freely behaving

16   larval zebrafish, which has ~ 100,000 neurons and can move two orders of magnitude

17   faster than *C. elegans*.

18

19   Tracking and whole brain imaging of naturally behaving zebrafish provides a new way to

20   study sensorimotor transformation across the brain circuit. A large body of research

21   suggests that sensory information processing depends strongly on the locomotor state of

22   an animal [36-38]. The ability to sense self-motion, such as proprioceptive feedback [39]

23   and efferent copy [40], can also profoundly shape the dynamics of the neural circuit and

24   perception. It would be ideal to have physiological access to *all* neurons in defined

1 behavioral states, where *all* sensory feedback loops remain intact and functional. Our

2 XLFM 3D tracking microscope is one step towards this goal, and our system would be

3 better exploited to explore the neural basis of more sophisticated natural behaviors, such

4 as prey capture and social interaction, where the integration of multiple sensory

5 feedbacks becomes critical.

6

7 The capability of XLFM can be further improved with the aid of technology development

8 in other areas. With more pixels on the imaging sensor, we can achieve even higher

9 spatial resolution without sacrificing imaging volume coverage by introducing more than

10 two different focal planes formed by more groups of microlenses. With better imaging

11 objective that can provide higher numerical aperture and larger field of view at the same

12 time, we can potentially image the entire nervous system of the larval zebrafish with

13 single neuron resolution in all three dimensions. Additionally, the high imaging speed of

14 XLFM holds the promise for recording electrical activity when high signal-to-noise

15 fluorescent voltage sensors become available [41]. Finally, the illumination-independent

16 characteristic of XLFM is perfectly suitable for recording brain activities from

17 bioluminescent calcium/voltage indicators in a truly natural environment, where the light

18 interference arising from fluorescence excitation can be eliminated [19].

19

1 **METHODS**

2 **XLFM**

3 The imaging system (Figure 1) was a customized upright microscope. Along the

4 fluorescence excitation light path, a blue laser (Coherent, OBIS 488 nm, 100 mW) was

5 expanded and collimated into a beam with a diameter of ~ 25 mm. It was then focused by

6 an achromatic lens (focal length: 125 mm) and reflected by an dichroic mirror (Semrock,

7 Di02-R488-25x36) into the back pupil of the imaging objective (Olympus,

8 XLPLN25XWMP2, 25X, NA 1.05, WD 2mm) to result in an illumination area of ~1.44

9 mm in diameter near the objective's focal plane. In fluorescence imaging light path, the

10 excited fluorescence was collected by the imaging objective and transmits through the

11 dichroic mirror. A pair of achromatic lenses (focal lengths: F1=180 mm & F2=160 mm),

12 arranged in 2F1+2F2 manner, was placed after the objective and dichroic mirror to

13 conjugate the objective's back pupil onto a customized lenslet array (Supplementary

14 Figure 1). The customized lenslet array was an aluminum plate with 27 holes (1 mm

15 diameter) housing 27 customized micro-lenses (focal length: 26 mm). 27 micro-lenses

16 were divided into two groups (Supplementary Figure 1) and an axial displacement of 2.5

17 mm was introduced between them. Due to the blockage of light by aluminum microlenses

18 housing, 16% of the light after 1.05 NA imaging objective is effectively collected by

19 camera. This efficiency is equivalent to using a 0.4 NA imaging objective. In the end, the

20 imaging sensor of a sCMOS camera (Hamamatsu, Orca-Flash 4.0 v2) was placed at the

21 middle plane between two focal planes formed by two different groups of micro-lenses.

22 The total magnification of the imaging system was ~ 4, so one camera pixel (6.5 μm)

23 corresponded to ~1.6 μm on the sample.

1

2 We developed a computational algorithm for 3D volume reconstruction. It requires an

3 accurately measured PSF (Supplementary Figure 2). The spatially invariant PSF was

4 measured by recording images of a 500 nm diameter fluorescent bead sitting on a

5 motorized stage under the objective. A stack of 200 images was recorded when the bead

6 was scanned with a step size of 2 μm in axial direction from 200 μm below the

7 objective's focal plane to 200 μm above. Since the images formed by two different

8 groups of micro-lenses were from different axial locations and have different

9 magnifications, the measured raw PSF data should be reorganized into two

10 complementary parts: PSF_A and PSF_B (Supplementary Figure 3 & 4), according to the

11 spatial arrangement of micro-lenses. We took PSF_A stack, PSF_B stack and a single

12 frame of raw image (2048 x 2048 pixels) as inputs, and applied Richard-Lucy

13 deconvolution to reconstruct the 3D volume.

14

15 **Image reconstruction of XLFM**

16 The underling framework of this new algorithm is developed from basic idea in Richard-

17 Lucy deconvolution. It starts with an estimation of the 3D fluorescent object:

$$Obj(x, y, z)$$

18 The algorithm assumes that the real 3D object can be approximated by a discrete number

19 of x-y planes at different axial z positions:

20 $$Obj(x, y, z) \sim Obj(x, y, z_k), \text{ where } k = 1, 2 .. n$$

21 The number and positions of these planes can be arbitrary, while, the Nyquist sampling

22 rate is usually chosen to optimize the speed and accuracy of the reconstruction.

23

1   Since the imaging system consists of two different groups of micro-lens, as shown in

2   Supplementary Figure 1, their PSFs (Supplementary Figure 3 & 4) each consists of a

3   stack of planes that are measured at same chosen axial positions z_k:

4 $$PSF_A(x, y, z_k) \ \& \ PSF_B(x, y, z_k)$$

5   Additionally, the images formed by two different groups of micro-lenses have different

6   magnifications, which can be determined experimentally. A ratio between two different

7   magnifications can be defined as:

$$\gamma = \frac{Magnification \ of \ group \ A \ microlenses}{Magnification \ of \ group \ B \ microlenses}$$

8   Then the captured image on the camera can be estimated as:

$$Img_{Est}(x, y) = \sum_{k=1}^{n} \{Obj_A(x, y, z_k) \otimes PSF_A(x, y, z_k) + Obj_B(x, y, z_k) \otimes PSF_B(x, y, z_k)\}$$

9 $$\text{Where, } Obj_A(x, y, z_k) = Obj_B(\gamma x, \gamma y, z_k)$$

10   The operator $\otimes$ represents 2D convolution.

11

12   The goal of the algorithm is to estimate the $Obj(x, y, z_k)$ from the measured camera

13   frame:

$$Img_{Meas}(x, y)$$

14   According to the algorithm of Richard-Lucy deconvolution, the iterative reconstruction

15   can be expressed as:

$$Img_{Est}^{i}(x, y) = \sum_{k=1}^{n} \{Obj_A^{i-1}(x, y, z_k) \otimes PSF_A(x, y, z_k) + Obj_B^{i-1}(x, y, z_k) \otimes PSF_B(x, y, z_k)\}$$

$$Obj_A^{tmp}(x, y, z_k) = Obj_A^{i-1}(x, y, z_k) \left\{ \frac{Img_{Meas}(x, y)}{Img_{Est}^{i}(x, y)} \otimes PSF_A(-x, -y, z_k) \right\}$$

$$Obj_B^{tmp}(x,y,z_k) = Obj_B^{i-1}(x,y,z_k)\left\{\frac{Img_{Meas}(x,y)}{Img_{Est}^i(x,y)}\otimes PSF_B(-x,-y,z_k)\right\}$$

$$Obj_A^i(x,y,z_k) = w(z_k)Obj_A^{tmp}(x,y,z_k) + (1-w(z_k))Obj_B^{tmp}(\gamma x,\gamma y,z_k)$$

$$Obj_B^i(x,y,z_k) = w(z_k)Obj_A^{tmp}\left(\frac{x}{\gamma},\frac{y}{\gamma},z_k\right) + (1-w(z_k))Obj_B^{tmp}(x,y,z_k)$$

1   Here $0 \le w(z_k) \le 1$ is the weighting factor at different axial positions. The choice of

2   $w(z_k)$ can be arbitrary. Due to the fact that the resolutions achieved by different groups

3   of lens at different z positions are not the same, the weighting factor can take this effect

4   into consideration and weights higher quality information more than the lower one. We

5   empirically choose $w(z_k)$ to optimize reconstruction quality and speed.

6

7   The starting estimation of the object can be any non-zeros value. Near the end of

8   iterations, $Obj_A^i(x,y,z_k)$ and $Obj_B^i(x,y,z_k)$ are interchangeable except with different

9   magnifications. Either of them can be used as the resulting estimate of the 3D object.

10

11   In XLFM, together with its reconstruction algorithm, the diffraction effect of the 3D light

12   field is properly taken into consideration by experimentally measured PSF. The captured

13   raw imaging data can be fed into the algorithm directly without any preprocessing. The

14   overlapping between sub-images formed by different micro-lenses is allowed

15   (Supplementary Figure 9) and the algorithm can automatically resolve the ambiguity

16   without affecting reconstructing performance. Due to this reason, the covered field of

17   view can be increased significantly. Based on the observation that additional changes of

18   estimated object became very small after 30 iterations, the reconstruction algorithm was

19   usually terminated after 30 iterations if there was no specific annotation. The

1   computation can speed up significantly by using GPU. It takes about 4 minutes to

2   reconstruct one 3D volume using desktop computer with a GPU (Nvidia Titan X). In

3   comparison, the reconstruction runs ~20X slower using CPU (Intel E5-2630v2) on a Dell

4   desktop.

5

6   The 3D deconvolution methods based on wave optics theory has been developed for

7   conventional LFM, but our methods differs from [21] in several ways: (1) the optical

8   imaging system is different. (2) The definitions of PSFs are different. Ours defines a

9   spatially *invariant* PSF, while [21] needs to define a spatially variant PSF, which could

10   lead to complexity in deconvolution algorithm and increased amount of computation. (3)

11   The PSF in [21] needs to be simulated based on a model of an ideal imaging system and

12   the assumption of monochromatic light, while ours can be measured experimentally and

13   takes all practical conditions, including imaging system and light properties, into

14   consideration.

15

16   **Resolution characterization of XLFM**

17   Unlike conventional microscopy, where the performance of the imaging system can be

18   fully characterized by PSF at the focal plane, the capability of XLFM is better described

19   as a function of positions throughout its imaging volume. By employing a state-of-art

20   objective, the imaging performance across the X-Y field of view is relatively uniform.

21   Here, we mainly focus on characterizing axial resolutions at different axial positions in

22   the whole imaging volume.

23

1   In our imaging system, each micro-lens is designed to have equivalent NA of 0.075, so

2   the resolution in X-Y plane is estimated to be 3.4 μm. The XLFM gains axial resolution

3   by viewing the object from large projection angles achieved by micro-lens sitting near the

4   edge of the objective's back pupil plane. For example, if two point light sources were

5   located at the same position in X-Y plane but were separated by Δz in axial direction, one

6   micro-lens in XLFM would capture an image of these two points with a shift between

7   them. The shift can be determined as:

$$d = \Delta z * tan\theta$$

8   Where θ is the inclination angle that can be inferred from measured PSF (Supplementary

9   Figure 2). If the two points in the image can be resolved, it means these two points

10   separated by Δz can be resolved by the imaging system. Since micro-lens sitting in the

11   outer layer of the array offers the largest inclination angle of 40 degree in our system, the

12   system's axial resolution dz can be directly calculated as:

$$dz = \frac{dxy}{tan\theta_{max}} = \frac{3.4\mu m}{tan(40°)} = 4\ \mu m$$

13   The best way to confirm the theoretical estimation is to image two fluorescent beads with

14   precisely controlled axial separations. But this is technically very challenging. Instead,

15   we pursued an alternative method that is equivalent to imaging two beads simultaneously:

16   (1) We first took a z stack of images of fluorescent beads, just like we do in measuring

17   PSF.

18   (2) In the post processing, we added two images taken at different z positions together to

19   mimic the situation that the beads were present simultaneously at two different *z*

20   positions.

1   Using this method, we could experimentally characterize the axial resolution at different

2   z positions.

3

4   To compare the experimental result with the theoretical prediction, we used a single

5   fluorescent bead with high SNR, as shown in Supplementary Figure 5a. We tested at

6   different axial positions of z=-100 µm , z=0 µm and z=100 µm , as shown in

7   Supplementary Figure 5b. The 3rd column shows the results by adding the two images in

8   the column 1 & 2 together. The capability of resolving two beads in the 3rd column can

9   be clearly seen by spatial frequency analysis, which is shown in the 4th column in

10   Supplementary Fig 5b. The two line dips, which indicate the existence of two beads

11   instead of one rod in the 4th column, are confirmations of the resolving capability. When

12   the two beads were separated by 5 µm, micro-lens 1 and 2 could well resolve them in the

13   range of $-100\,\mu m \leq z \leq 0$ and $0 \leq z \leq 100\,\mu m$, respectively. The complementary

14   information provided by the two groups of lens makes the whole system capable of

15   maintaining high axial resolution of 5 µm across a 200 µm depth.

16

17   Although experimentally measured axial resolution was slightly lower than the

18   theoretical prediction of 4µm, the experimental data could describe more accurately the

19   resolution change along different axial positions. To better estimate the system

20   performance in practical conditions, we used a sample of densely packed 0.5µm diameter

21   fluorescent beads with moderate SNR, as shown in Supplementary Figure 6a. 5 µm axial

22   resolution could still be preserved across a depth of 100 µm. The resolution decayed

1   gradually to ~10 μm at the edge of an imaging volume with 400 μm axial coverage, as

2   shown in Supplementary Figure 6b.

3

4   In vivo resolution characterization is challenging due to lack of bright and spot like

5   features in living animals. Additionally, the achievable resolution depends on optical

6   properties of biological tissues, which can be highly heterogeneous and difficult to infer.

7   The light scattering and aberration induced by biological tissue usually leads to degraded

8   imaging performance [28, 42-44].

9

10   **XY tracking system**

11   To compensate lateral fish movement and to retain the entire fish head within the field of

12   view of a high NA objective (25x, NA =1.05), a high speed camera captured fish motion

13   (500 fps, Basler aca2000-340kmNIR) and we developed an FPGA-based RT system in

14   LabVIEW that can rapidly identify the head position by processing the pixel stream data

15   within the Cameralink card before the whole image was transferred to RAM. The error

16   signal between the actual head position and the set point was then fed into PID to

17   generate output signals and to control the movement of a high-speed motorized stage (PI

18   M687 ultrasonic linear motor stage). In the case of large background noise, we

19   alternatively performed conventional imaging processing in C/C++ (within 1 ms delay).

20   The rate-limiting factor of our lateral tracking system was the response time of the stage

21   (~ 300 Hz).

22

Autofocus system

We applied the principle of LFM to determine the axial movement of larval zebrafish. The autofocus camera behind a one-dimensional microlens array captured triplet images of the fish from different perspectives (Supplementary Figure 8a). Z motion caused an extension or contraction between the centroids of the fish head in the left and right sub-images, an inter-fish distance (Supplementary Figure 8b) that can be accurately computed from image autocorrelation. The inter-fish distance, multiplied by a pre-factor, can be used to estimate the z position of the fish, for it varies linearly with axial movement (Supplementary Figure 8c). The error signal between the actual axial position of the fish head and the set point was then fed into PID to generate an output signal to drive a piezo-coupled fish container. The feedback control system was written in LabVIEW. The code was further accelerated by parallel processing and the closed loop delay is ~ 5 ms. The rate-limiting factor of the autofocus system was the settling time of the piezo scanner (PI P725KHDS, 400 μm travelling distance), which was about 10 ms.

Real-time Behavioral Analysis

Two high-speed cameras acquired dark-field images at high and low magnification respectively, and customized machine vision software written in C/C++ with the aid of OpenCV library was dedicated to perform real-time behavioral analysis of freely swimming larval zebrafish. At high magnification, eye positions, their orientation and convergence angle were computed; at low magnification, the contour of the whole fish, the centerline, body curvature as well as bending angle of the tail were computed. The

1 high mag RT analysis was running at ~ 120 fps and the low mag RT analysis was running

2 at ~ 180 fps.

3

4 **Zebrafish sample preparation**

5 All larval zebrafish (huc:h2b-gcamp6f and huc:gcamp6s) were raised in embryo medium

6 under 28.5 ℃ and 14/10 hours light/dark cycle. Zebrafish were fed with paramecium

7 since 4 days post-fertilization (dpf). For restrained experiments, 4-6 dpf zebrafish were

8 embedded in 1% low melting point agarose. For freely moving experiments, 7-11 dpf

9 zebrafish with 10% Hank's solution were transferred in a customized chamber (20 mm in

10 diameter, 0.8 mm in depth), and 10-20 paramecia were added before the chamber is

11 covered by a coverslip. All animal handlings were approved by the Institute of

12 Neuroscience, Chinese Academy of Sciences.

13

14 **Neural activities analysis**

15 To extract visual stimuli correlated neural activities shown in Figure 1e & f, the time

16 series of 3D volume stacks were first converted to one 3D volume stack of same size.

17 Each voxel in the converted 3D volume stack represents the variance of voxel values over

18 time. Then, the neuron candidates are extracted by identifying local maxima in the

19 converted 3D volume stack. Since the size of single neuron can be determined

20 empirically, the size of Region-Of-Interest (ROI) was set accordingly. Using fixed ROI

21 size, the voxels around local maxima were selected to represent neurons spatially. In the

22 end, the fluorescence intensity signals over each neuron's ROI were integrated and

23 extracted as neural activities. To identify visual stimuli correlated neural activities, the

1   neural activities $\Delta F/F_0$ were normalized to their maximum calcium response $\Delta F_{max}/F_0$

2   over time and sorted according to their onset time when ΔF first reaches 20% of its

3   ΔF_{max} (Figure 1e & f) after visual stimuli.

4

5

6 **References:**

7   1.   Kerr, J.N.D. and W. Denk, *Imaging in vivo: watching the brain in action.* Nature
8   Reviews Neuroscience, 2008. **9**(3): p. 195-205.
9   2.   Dombeck, D.A., et al., *Imaging large-scale neural activity with cellular*
10   *resolution in awake, mobile mice.* Neuron, 2007. **56**(1): p. 43-57.
11   3.   Wyart, C., et al., *Optogenetic dissection of a behavioural module in the vertebrate*
12   *spinal cord.* Nature, 2009. **461**(7262): p. 407-U105.
13   4.   Boyden, E.S., et al., *Millisecond-timescale, genetically targeted optical control of*
14   *neural activity.* Nature Neuroscience, 2005. **8**(9): p. 1263-1268.
15   5.   Zhang, F., et al., *Multimodal fast optical interrogation of neural circuitry.* Nature,
16   2007. **446**(7136): p. 633-U4.
17   6.   Chen, T.W., et al., *Ultrasensitive fluorescent proteins for imaging neuronal*
18   *activity.* Nature, 2013. **499**(7458): p. 295-+.
19   7.   Tian, L., et al., *Imaging neural activity in worms, flies and mice with improved*
20   *GCaMP calcium indicators.* Nature Methods, 2009. **6**(12): p. 875-U113.
21   8.   Luo, L., E.M. Callaway, and K. Svoboda, *Genetic dissection of neural circuits.*
22   Neuron, 2008. **57**(5): p. 634-660.
23   9.   Friedrich, R.W., G.A. Jacobson, and P. Zhu, *Circuit neuroscience in zebrafish.*
24   Curr Biol, 2010. **20**(8): p. R371-81.
25   10.   Ahrens, M.B. and F. Engert, *Large-scale imaging in small brains.* Curr Opin
26   Neurobiol, 2015. **32**: p. 78-86.
27   11.   Ahrens, M.B., et al., *Brain-wide neuronal dynamics during motor adaptation in*
28   *zebrafish.* Nature, 2012. **485**(7399): p. 471-7.
29   12.   Ahrens, M.B., et al., *Whole-brain functional imaging at cellular resolution using*
30   *light-sheet microscopy.* Nat Methods, 2013. **10**(5): p. 413-20.
31   13.   Engert, F., *The big data problem: turning maps into knowledge.* Neuron, 2014.
32   **83**(6): p. 1246-8.
33   14.   Engert, F., *Fish in the matrix: motor learning in a virtual world.* Front Neural
34   Circuits, 2012. **6**: p. 125.
35   15.   Bianco, I.H., et al., *The tangential nucleus controls a gravito-inertial vestibulo-*
36   *ocular reflex.* Curr Biol, 2012. **22**(14): p. 1285-95.
37   16.   Bianco, I.H., A.R. Kampff, and F. Engert, *Prey capture behavior evoked by*
38   *simple visual stimuli in larval zebrafish.* Front Syst Neurosci, 2011. **5**: p. 101.
39   17.   Patterson, B.W., et al., *Visually guided gradation of prey capture movements in*
40   *larval zebrafish.* J Exp Biol, 2013. **216**(Pt 16): p. 3071-83.

18. Trivedi, C.A. and J.H. Bollmann, *Visually driven chaining of elementary swim patterns into a goal-directed motor sequence: a virtual reality study of zebrafish prey capture.* Front Neural Circuits, 2013. **7**: p. 86.

19. Naumann, E.A., et al., *Monitoring neural activity with bioluminescence during natural behavior.* Nat Neurosci, 2010. **13**(4): p. 513-20.

20. Muto, A., et al., *Real-time visualization of neuronal activity during perception.* Curr Biol, 2013. **23**(4): p. 307-11.

21. Broxton, M., et al., *Wave optics theory and 3-D deconvolution for the light field microscope.* Opt Express, 2013. **21**(21): p. 25418-39.

22. Prevedel, R., et al., *Simultaneous whole-animal 3D imaging of neuronal activity using light-field microscopy.* Nat Methods, 2014. **11**(7): p. 727-30.

23. Pégard, N.C., et al., *Compressive light-field microscopy for 3D neural activity recording.* Optica, 2016. **3**(5): p. 517-524.

24. Severi, K.E., et al., *Neural control and modulation of swimming speed in the larval zebrafish.* Neuron, 2014. **83**(3): p. 692-707.

25. Adelson, E.H. and J.Y.A. Wang, *Single Lens Stereo with a Plenoptic Camera.* Ieee Transactions on Pattern Analysis and Machine Intelligence, 1992. **14**(2): p. 99-106.

26. Abrahamsson, S., et al., *Fast multicolor 3D imaging using aberration-corrected multifocus microscopy.* Nat Meth, 2013. **10**(1): p. 60-63.

27. Perwass, C. and L. Wietzke. *Single lens 3D-camera with extended depth-of-field.* 2012.

28. Ji, N., *Adaptive optical fluorescence microscopy.* Nat Meth, 2017. **14**(4): p. 374-380.

29. Semmelhack, J.L., et al., *A dedicated visual pathway for prey detection in larval zebrafish.* Elife, 2014. **3**.

30. Bianco, I.H. and F. Engert, *Visuomotor transformations underlying hunting behavior in zebrafish.* Curr Biol, 2015. **25**(7): p. 831-46.

31. Venkatachalam, V., et al., *Pan-neuronal imaging in roaming Caenorhabditis elegans.* Proc Natl Acad Sci U S A, 2016. **113**(8): p. E1082-8.

32. Nguyen, J.P., et al., *Whole-brain calcium imaging with cellular resolution in freely behaving Caenorhabditis elegans.* Proc Natl Acad Sci U S A, 2016. **113**(8): p. E1074-81.

33. Berg, H.C., *How to Track Bacteria.* Review of Scientific Instruments, 1971. **42**(6): p. 868-&.

34. Ng, R., et al., *Light Field Photography with a Hand-held Plenoptic Camera.* Stanford Tech Report 2005.

35. Levoy, M., et al., *Light field microscopy.* ACM Trans. on Graphics (Proc. SIGGRAPH), 2006. **25**: p. 924-934.

36. Niell, C.M. and M.P. Stryker, *Modulation of visual responses by behavioral state in mouse visual cortex.* Neuron, 2010. **65**(4): p. 472-9.

37. Maimon, G., A.D. Straw, and M.H. Dickinson, *Active flight increases the gain of visual motion processing in Drosophila.* Nat Neurosci, 2010. **13**(3): p. 393-9.

38. Chiappe, M.E., et al., *Walking modulates speed sensitivity in Drosophila motion vision.* Curr Biol, 2010. **20**(16): p. 1470-5.

1 39. Pearson, K.G., *Proprioceptive regulation of locomotion.* Current Opinion in
2   Neurobiology, 1995. **5**(6): p. 786-791.
3 40. Bell, C.C., *An Efference Copy Which Is Modified by Reafferent Input.* Science,
4   1981. **214**(4519): p. 450-453.
5 41. St-Pierre, F., et al., *High-fidelity optical reporting of neuronal electrical activity*
6   *with an ultrafast fluorescent voltage sensor.* Nat Neurosci, 2014. **17**(6): p. 884-9.
7 42. Ji, N., D.E. Milkie, and E. Betzig, *Adaptive optics via pupil segmentation for*
8   *high-resolution imaging in biological tissues.* Nat Meth, 2010. **7**(2): p. 141-147.
9 43. Wang, K., et al., *Rapid adaptive optical recovery of optimal resolution over large*
10   *volumes.* Nat Meth, 2014. **11**(6): p. 625-628.
11 44. Wang, K., et al., *Direct wavefront sensing for high-resolution in vivo imaging in*
12   *scattering tissue.* Nature Communications, 2015. **6**: p. 7276.
13
14

Acknowledgements

1 ## Supplementary Videos:

2 **Supplementary Video 1| Whole brain functional imaging of larval zebrafish under**

3 **light stimulation**

4 Whole brain XLFM imaging of a 5 dpf agarose-embedded larval zebrafish expressing

5 nucleus-localized GCamp6f. Light stimulation was introduced at time point t=0. Whole

6 brain activities was recorded at 77 volumes/s.

7

8 **Supplementary Video 2| Whole brain functional imaging of larval zebrafish's**

9 **spontaneous activities**

10 Whole brain XLFM imaging of a 5 dpf agarose-embedded larval zebrafish expressing

11 nucleus-localized GCamp6f. Spontaneous neural activities were recorded at 0.6

12 volumes/s.

13

14 **Supplementary Video 3| Whole brain functional imaging of larval zebrafish's**

15 **spontaneous activities**

16 Whole brain XLFM imaging of a 5 dpf agarose-embedded larval zebrafish expressing

17 cytoplasm-labeled GCamp6s. Spontaneous neural activities were recorded at 0.6

18 volumes/s.

19

20 **Supplementary Video 4| Whole brain functional imaging of larval zebrafish under**

21 **light stimulation**

22 Whole brain XLFM imaging of a 5 dpf agarose-embedded larval zebrafish expressing

23 cytoplasm-labeled GCamp6s. Light stimulation was introduced at time point t=0. Whole

1   brain activities were recorded at 50 volumes/s.

2

3   **Supplementary Video 5| Tracking of larval zebrafish during prey capture behavior**

4   **at low resolution**

5   Tracking and real time kinematic analysis of larval zebrafish during prey capture

6   behavior at low resolution. Recorded at 190 frames per second.

7

8   **Supplementary Video 6| Tracking of larval zebrafish during prey capture behavior**

9   **at high resolution**

10 Tracking and real time kinematic analysis of larval zebrafish during prey capture

11 behavior at high resolution. Recorded at 160 frames per second.

12

13 **Supplementary Video 7| Whole brain functional imaging of a freely swimming**

14 **larval zebrafish under light stimulation**

15 Whole brain XLFM imaging of a 7 dpf freely swimming larval zebrafish expressing

16 cytoplasm-labeled GCamp6s. Light stimulation was introduced at time point t=0. Whole

17 brain activities were recorded at 77 volumes/s and with flashed excitation laser of 0.3 ms

18 exposure time.

19

20 **Supplementary Video 8| Whole brain functional imaging of a freely swimming**

21 **larval zebrafish during prey capture behavior**

22 Whole brain XLFM imaging of an 11 dpf freely swimming larval zebrafish expressing

23 cytoplasm-labeled GCamp6s. The entire process during which the larval zebrafish caught

1   and ate the paramecium was recorded.

2

3   **Supplementary Video 9| Whole brain functional imaging of a freely swimming**

4   **larval zebrafish during prey capture behavior**

5   Whole brain XLFM imaging of a 7 dpf freely swimming larval zebrafish expressing

6   nucleus-localized GCamp6f. The entire process during which the larval zebrafish caught

7   and ate the paramecium was recorded.

8

1 **Supplementary Figures:**

2 **Supplementary Figure 1| Customized lenslet array**

3

Group A micro-lenses
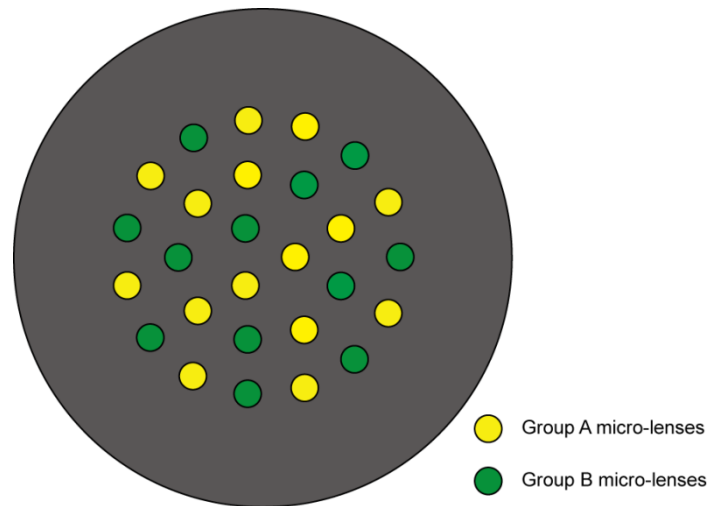
Group B micro-lenses

4 Customized lenslet array consist of 27 customized micro-lenses (1mm diameter, 26 mm

5 focal length) embedded in an aluminum plate. Micro-lenses were divided into two groups

6 (A or B), illustrated by yellow and green color respectively.

7

1 **Supplementary Figure 2| Experimentally measured PSF of the whole imaging**

2 **system**
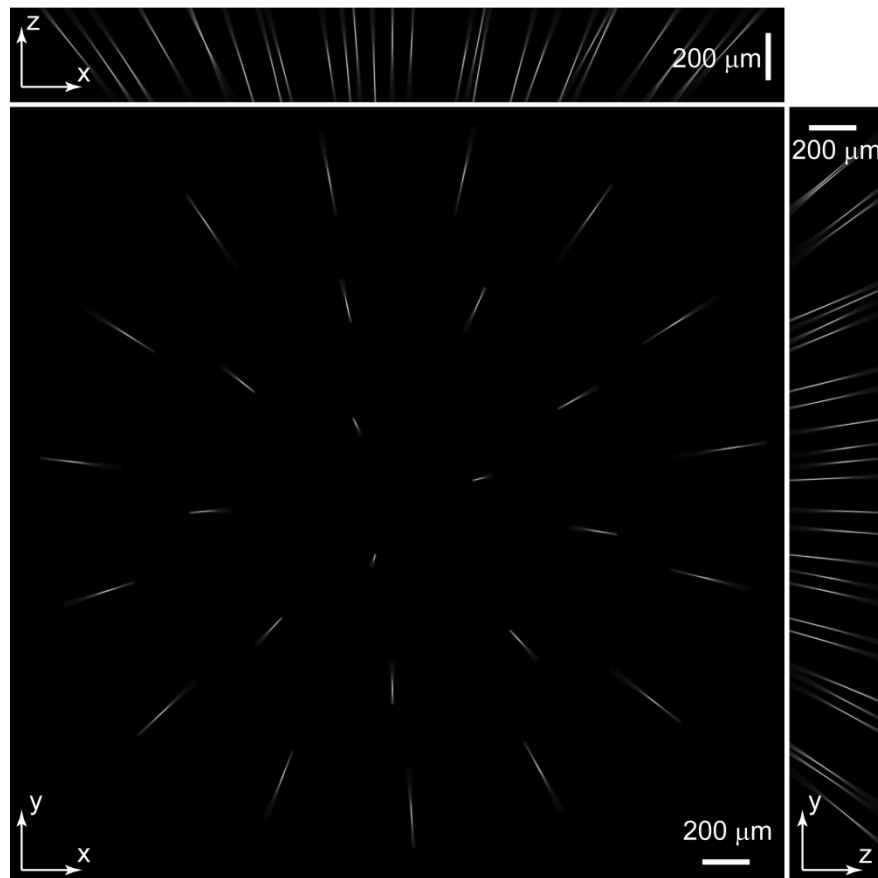
3

4 Maximum Intensity Projections (MIPs) of the measured raw PSF stack. The stack has a

5 size of 2048 pixels x 2048 pixels x 200 pixels with voxel size of 1.6 μm x 1.6 μm x 2 μm.

6

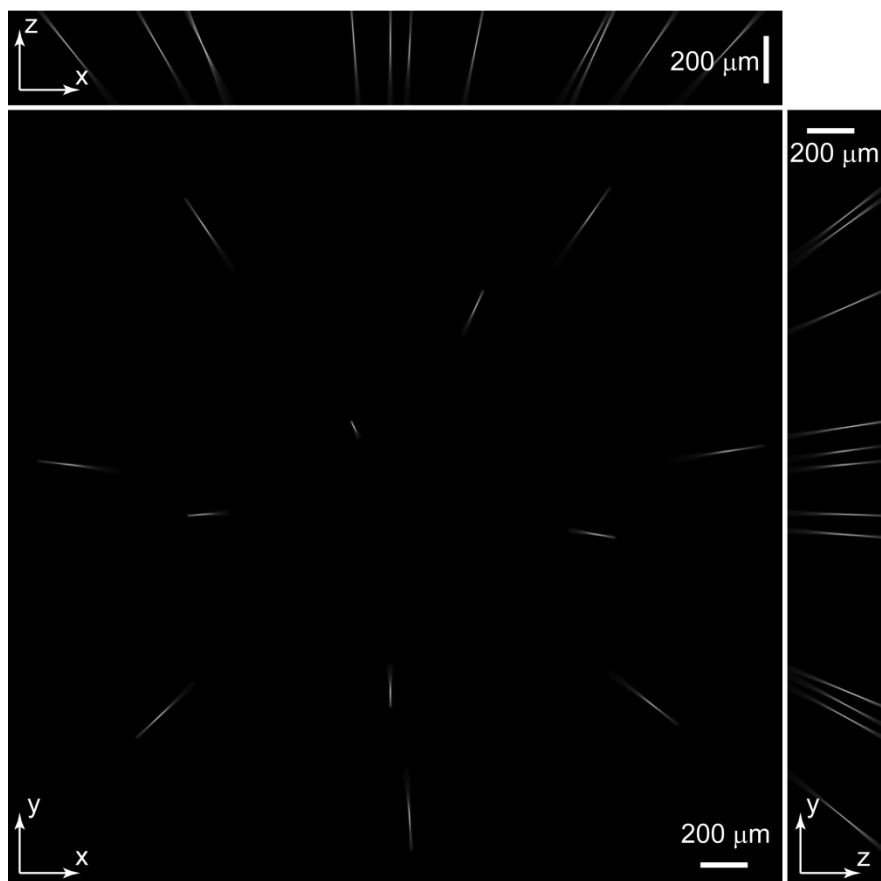1   **Supplementary Figure 3| PSF of the Group A micro-lenses: PSF_A**

2
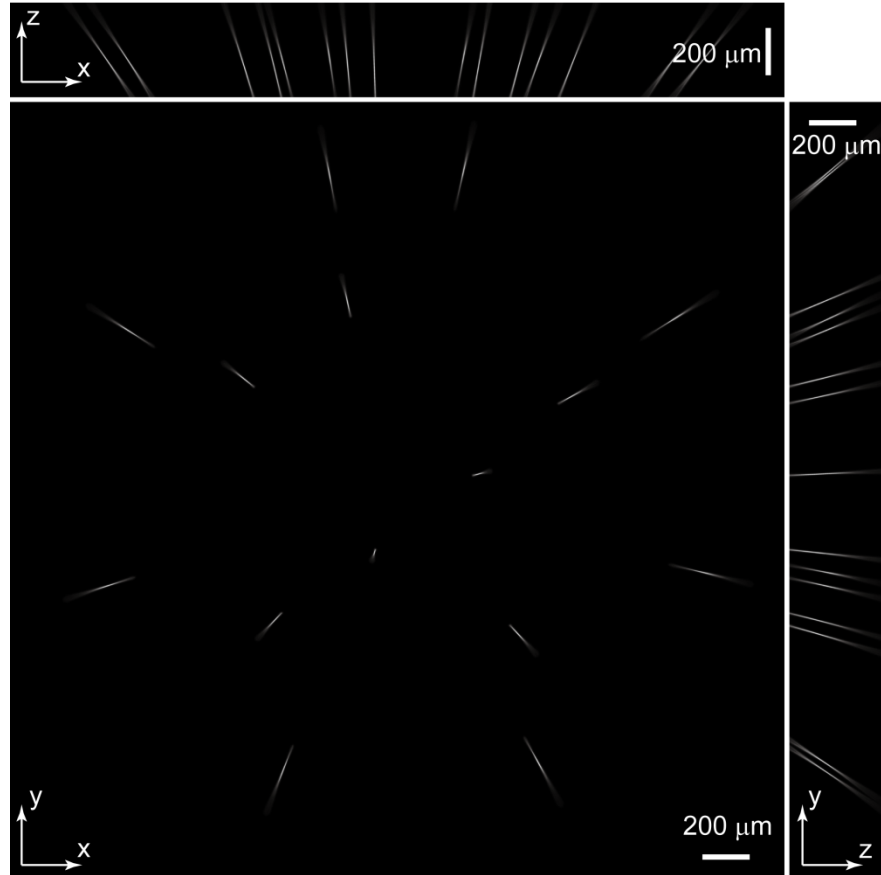
3   Maximum Intensity Projections (MIP) of PSF_A. PSF_A was extracted from

4   experimentally measured PSF (Supplementary Figure 2) according to individual micro-

5   lens' positions in group A.

6

1   **Supplementary Figure 4| PSF of the Group B micro-lenses: PSF_B**

2

3   Maximum Intensity Projections (MIP) of PSF_B. PSF_B was extracted from

4   experimentally measured PSF (Supplementary Figure 2) according to individual micro-

5   lens' positions in group B.

6

1 **Supplementary Figure 5|Characterization of axial resolution of XLFM at high SNR**


2
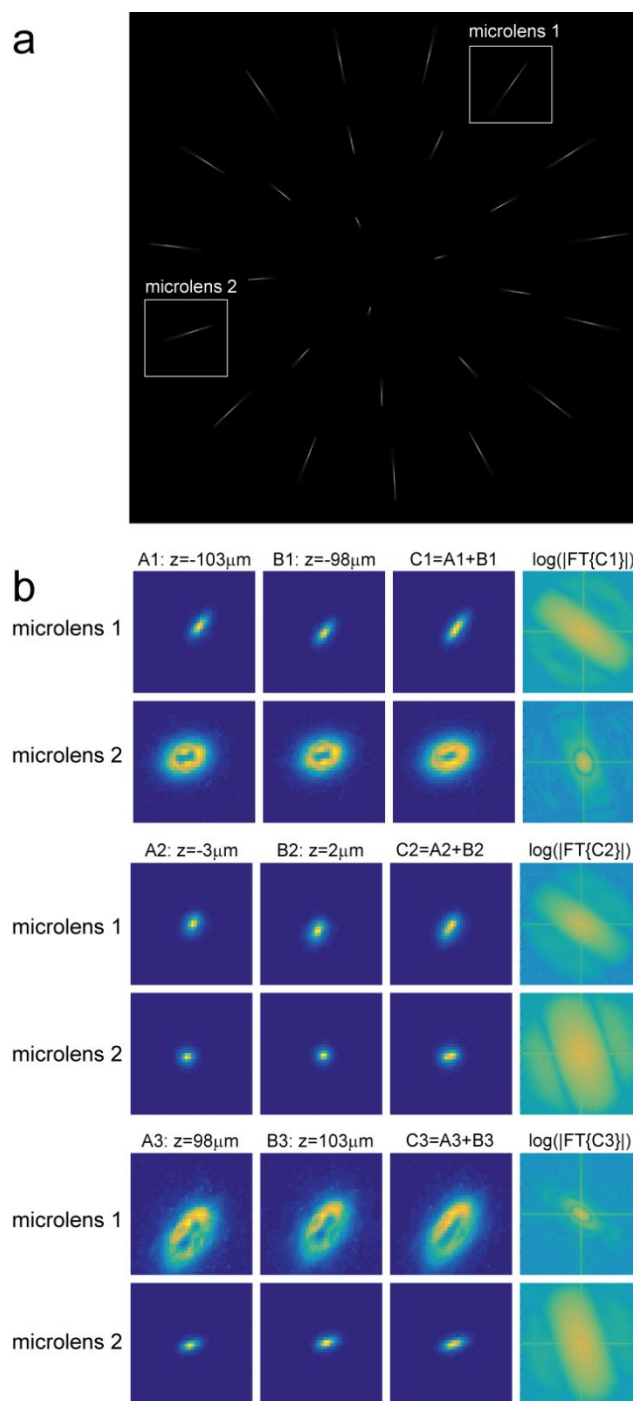
3 Characterization of axial resolution using a 0.5µm diameter bright fluorescent particle (a)

4 Maximum intensity projection of an image stack consisting of particle's fluorescent

5 images captured at different z positions. (b) Analysis of images formed by micro-lens 1

1   and 2, indicated by sub-regions as shown in (a). The 1st and 2nd columns are the

2   particle's fluorescent images captured at different z positions that are separated by 5μm.

3   The 3rd column is the sum of column 1 and 2. The 4th column is the Fourier analysis of

4   column 3 using function: $f(x) = \log(|\mathcal{F}(x)|)$, where $\mathcal{F}(x)$ represents Fourier Transform.

5

1 **Supplementary Figure 6|Characterization of axial resolution of XLFM at low SNR**

2
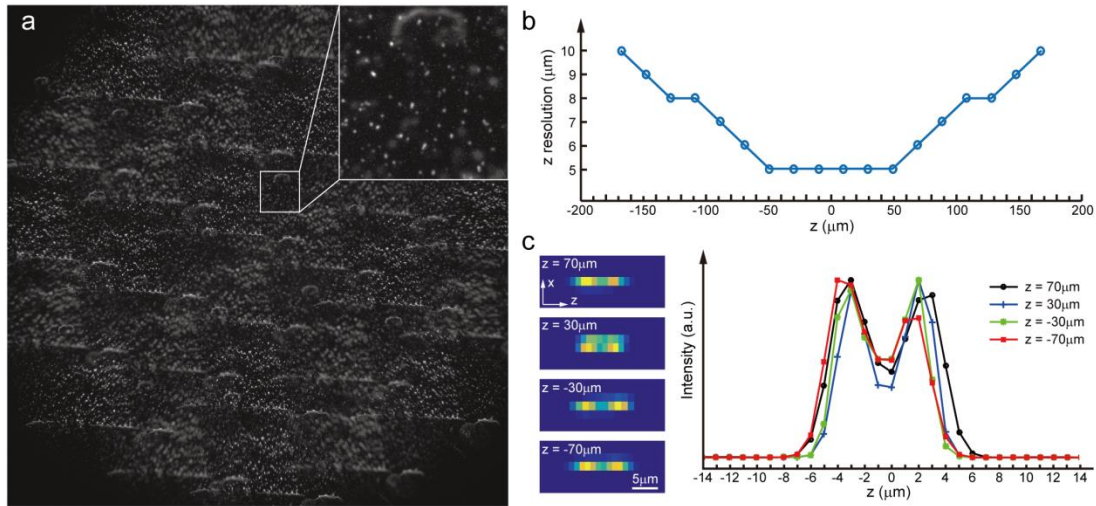
3   Characterization of axial resolution using densely packed fluorescent particles (0.5μm in

4   diameter) at low SNR. (a) Sample image from an image stack of fluorescent particles

5   captured at different z positions. (b) Axial resolution at different depth characterized by

6   finding the minimum separation of two particles in z, which can be well resolved using

7   the reconstruction algorithm (Supplementary Note 1). (c) Left, reconstructed examples of

8   X-Z projections of two particles located at different z positions (-70 μm, -30 μm , 30 μm ,

9   70 μm) with different axial separations (6 μm, 5 μm , 5 μm , 6 μm); right, extracted

10 intensity profiles of these examples.

11

1   **Supplementary Figure 7| Characterization of photo bleaching effect in fluorescence**

2   **imaging by XLFM**
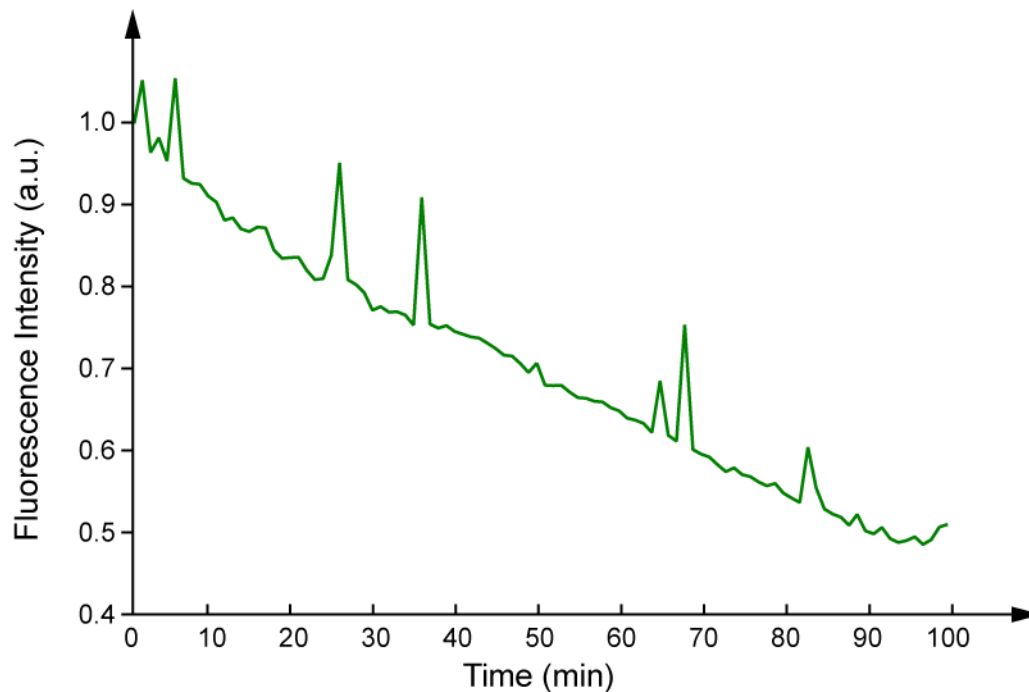
3

4   Photo-bleaching effect was characterized by total fluorescence intensity change of a 7dpf

5   zebrafish larval with nucleus-localized GCamp6f. The fish was embedded in 1% agarose

6   and was continuously exposed to 2.5mW/mm^2 fluorescence excitation laser (488nm)

7   illumination. After ~100 minutes, corresponding to 300,000 volumes when volume rate is

8   50 volumes/s, the fluorescence intensity dropped to half of that at the starting point. The

9   random peaks appearing in the curve corresponded to spontaneous neural activities. The

10   fish was alive and swam normally when it was relieved from agarose after imaging.

11

1 **Supplementary Figure 8| Characterization of the autofocus system**

2
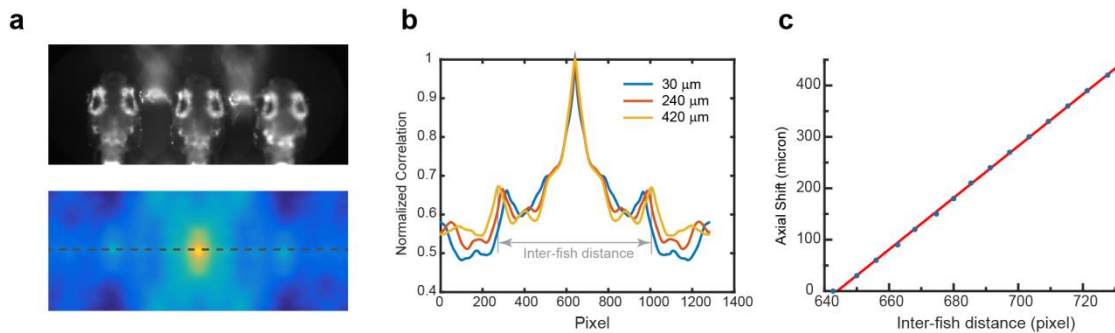
3

4 (a) Autofocus camera behind a one-dimensional lenslet array captured triplet images of

5 fish head (up). Its autocorrelation function was computed (bottom). (b)The central line

6 profile of the autocorrelation function was extracted and the inter-fish distance was
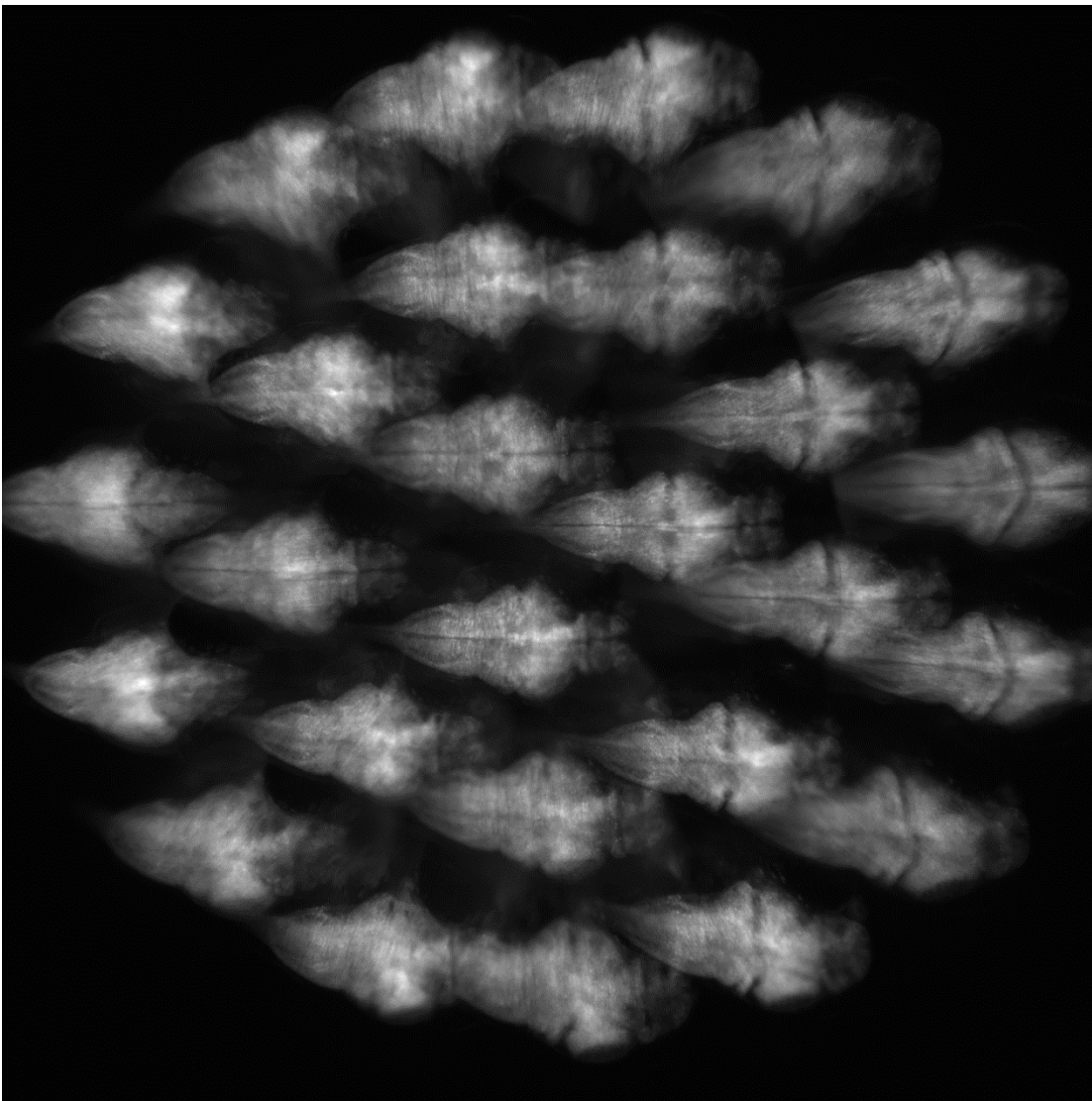
7 computed by finding the local maximums in the autocorrelation function. (c) The Axial

8 shift of fish head, calibrated by moving the piezo at constant interval, fit linearly (red line)

9 with the inter-fish distance.

10

1   **Supplementary Figure 9| Example of camera captured raw imaging data of larval**

2   **zebrafish.**

3

4   Raw fluorescence imaging data consists of 27 sub-images of a larval zebrafish formed by

5   27 micro-lenses. The overlaps between sub-images were allowed and the reconstruction

6   algorithm can automatically resolve this problem without affecting imaging performance.

7

1 **Supplementary Table**

2 **Acquisition parameters for fluorescence imaging**

	Zebrafish lines	Age (dpf)	Volume rate (Hz)	Flash laser exposure time (ms)	Average laser illumination intensity (mW/mm2)
Figure 1	huc:h2b-gcamp6f	5	77	13	2.5
Figure 3	huc:gcamp6s	11	50	1	2.8
Supplementary Video 1	huc:h2b-gcamp6f	5	77	13	2.5
Supplementary Video 2	huc:h2b-gcamp6f	5	0.6	300	0.5
Supplementary Video 3	huc:gcamp6s	5	0.6	100	0.37
Supplementary Video 4	huc:gcamp6s	6	50	20	0.37
Supplementary Video 7	huc:gcamp6s	7	77	0.3	1.3
Supplementary Video 8	huc:gcamp6s	11	50	1	2.8
Supplementary Video 9	huc:h2b-gcamp6f	7	77	0.2	0.9

3

1